Aerospace Science and Technology 102 (2020) 105869

Contents lists available at ScienceDirect

Aerospace Science and Technology

www.elsevier.com/locate/aescte

Revisiting slug calorimeters for hypersonics

J.I. Frankel [a,*], K. Ekici [b]

[a] New Mexico State University, United States of America
[b] University of Tennessee, Knoxville, United States of America

ARTICLE INFO

Article history:
Received 31 January 2020
Received in revised form 29 March 2020
Accepted 30 March 2020
Available online 21 May 2020
Communicated by Cummings Russell

Keywords:
Heat flux
Slug calorimeter
Volterra equation
Data reduction equations

ABSTRACT

This paper describes the first steps toward developing a highly-accurate multi-layered slug calorimeter for estimating the surface heat flux in high-enthalpy flows associated with hypersonic ground test campaigns. Slug geometry, material choices, test conditions, manufacturing method, mathematical modeling and instrumentation selection must be integrated into the design process in order to achieve the desired accuracy outcome. Integration is often overlooked in lieu of simplified data reduction equations that relate in-depth temperature measurements to the desired surface heat flux. Simplified models are often physics deficient and can lead to misleading interpretations. This paper illustrates the need for inclusive modeling in arriving at the data reduction equation for the heat flux gauge. Several important results are highlighted in this paper including the: (a) identification of data reduction model discrepancies; (b) significance of Volterra integral formulations for algorithm development; (c) implementation of a parameter-free preconditioner operated on data reduction model for low-pass filtering; (d) development of the approximation thread for uncertainty propagation; (e) achievement of stability through the future-time method; and, (f) extraction of the optimal regularization parameter through phase-plane and cross-correlation concepts for estimating the "best" heat flux.

1. Introduction

This paper proposes a technical pathway toward reconstructing the surface (net) heat flux for a newly proposed multi-layered slug calorimeter. Slug calorimeters [1–7] are fundamental gauges for estimating heat flux [8,9]. The rudimentary gauge provides fundamental insight into an energy balance; and, further illustrates the concept of a data reduction equation based on simple input-output principles. In this case, the input is the surface heating source while the output is the measured slug "bulk" temperature. The measured in-depth slug temperature is assumed as the "bulk" value. Unfortunately, this simple data reduction equation is computationally unstable due to its mathematical structure involving time differentiation of the measured (non-perfect) discrete temperature. Thus, the data reduction process involves a violation of well-posedness [10,11].

The rudimentary gauge involves a slug of a material that is encapsulated in an ideal insulator (adiabatic condition) where a single surface is exposed to the heating source. From first principles, the imparted surface energy is related to the storage of energy. Unfortunately, many assumptions are contained in this simplified formulation. In forward/direct problems [8,9], the input (i.e., heat flux) is given and the output (i.e., temperature history) is determined. This seemingly simple reversal leads to an inverse problem [12–14]. This class of problem is ill posed [10,11]. That is, noise in the measured data amplifies the error in the response which worsen with increasing sampling rate. Simplified models put severe constraints on the design of the sensor for maintaining idealized system boundary conditions. Further, the measured temperature at fixed position is not truly equal to the "bulk" temperature described in the data reduction equation. Finally, it should be remarked that the temperature measuring sensor possesses its own intrusive characteristics that produce time delays and attenuation effects [15,16].

---

* Corresponding author.
E-mail addresses: jfranke1@utk.edu (J.I. Frankel), ekici@utk.edu (K. Ekici).

https://doi.org/10.1016/j.ast.2020.105869

Nomenclature

a	constant,	$\text{s}^{-1/2}$
A	cross sectional area,	m^2
b	constant,	$\text{K-m}^2/\text{J}$
c	specific heat capacity,	J/(kg-K)
$\widehat{c}$	specific heat capacity,	J/(kg-K)
$\dot{E}$	Energy per unit time,	W
f_s	sampling frequency,	Hz
k	thermal conductivity,	W/(m-K)
L_1	length,	m
M_f	multiplication factor	
N	number of data points beyond the initial condition	
P	maximum number of future-time parameters	
q''	heat flux,	W/m^2
q''_s	source heat source,	W/m^2
$\tilde{q}''_{s,\eta_1,\gamma_m,N}$	approximate source heat flux,	W/m^2
r	constant,	1/K
$R(q'')$	cross-correlation coefficient for heat flux	
$R(dq''/dt)$	cross-correlation coefficient for heat flux rate	
t	time,	s
t_{max}	maximum data collection time,	s
T	lumped temperature,	K
T^*	distributed temperature,	K
T_o	initial temperature,	K
T_r	reference temperature,	K
u	dummy time variable,	s
x	spatial coordinate,	m
Greek		
α	thermal diffusivity,	m^2/s
β	thermal effusivity,	$\text{W-}\sqrt{s}/(\text{m}^2\text{-K})$
Δt	time sampling intervals,	s
$\epsilon_{q,m}$	heat flux RMS error,	W/cm^2
γ	continuous future-time parameter,	s
γ_m	discrete future-time parameter,	s
η_1	probe location,	m
θ	reduced temperature,	$T - T_o$, °C, K
ρ	density,	kg/m^3

Flow characterization is key in high enthalpy facilities for (i) new material development associated with thermal protection systems (TPS's); and, (ii) code validation studies for modeling purposes. New hypersonic test facilities are being introduced world wide. However, significantly less effort has been directed toward heat flux sensor development. This paper provides the primary steps for developing a cold or explosively bonded, multilayered slug calorimeter that can be developed using various backside boundary conditions (i.e., insulated or cooled). This initial paper focuses on analytical developments in order to display and clarify physical deficiencies associated with the produced data reduction equation. With this initial analysis, a plan is suggested for achieving the desired accuracy goals. The approach takes advantage of physics; materials; connectivity of materials; analysis tools; computational tools; experimental design and instrumentation; and, insight. References [17,18] and the classical Schultz and Jones [19] AGARD report (with noted corrections [20,21]) detail previous methods for analyzing measured data for this style of heat flux gauge. These reported methods serve as a baseline for developing the preconditioned integral equation proposed here. References [17] and [18] provide background and clarity for developing preconditioned equations.

Section 2 provides the mathematical formulation of the data reduction equation based on a set of assumptions. Section 3 describes the regularization and numerical methods used for producing a family of heat flux predictions based on the regularization parameter. Section 4 provides numerical results comparing models and identify physics deficiency as well as describing the means for estimating the optimal heat-flux prediction. Section 5 presents some concluding remarks and makes recommendations for the next progressive step.

2. Formulation of data reduction equation

This section provides the analytic derivation leading to a new data reduction equation for estimating the net surface heat flux, $q''(0,t)$ into the proposed multi-layered calorimeter. This initial model helps define the analytic process and necessary numerical toolset for a new generation of calorimeters. Fig. 1a displays a heat flux source, $q''_s(t)$ impinging the front face of a "slug" at $x = 0$ while all other surfaces (sides and back) are assumed adiabatic ($substrate : k_2 = 0$ W/(m-K)). The two-region problem is defined using a high-thermal conductivity, high-thermal diffusivity slug (Region 1) ideally adhered to an adiabatic substrate (Region 2). For this case, Region 1 is modeled as a slug (spatially lumped (L) mass) where a single time-varying temperature is produced. When the thermophysical properties are assumed constant, the modeled temperature is representative of the average temperature in the slug. However, when instrumentating the slug, say using a thermocouple located at $x = \eta_1 < L_1$, the measured temperature is not identically the average temperature. This can introduce a bias. Further, if the product of density and specific heat (i.e., $\rho_1 \widehat{c}_1(T_1^*(x,t))$) is temperature dependent then the lumped temperature is approximated as the average temperature, $\bar{T}_1(t)$. Here, $T_1^*(x,t)$ is the temperature associated with a fully distributed (D) solution in Region 1.

Typical calorimeters are based on Fig. 1a for producing a simplified data reduction equation. However, substantial onus is now placed on designing and fabricating a gauge that meets the adiabatic constraints (e.g., [6]). In reality, this is a difficult task as an adiabatic surface does not exist. Some extended models possessing a "heat loss term" have been suggested [7] in order to retain the simplified ordinary differential equation form. The large testing space involving temperature range, heat flux, and test duration further complicates the functionality of the sensor. Shock and expansion tunnel experiments involve small temperature rises and short test times while arc-jet experiments may involve large temperature spans at either short- or long-time exposures.

Fig. 1b displays the next step toward reality as the adiabatic backside is replaced with a substrate of low thermal conductivity ($k_2 > 0$ W/(m-K)) while maintaining adiabatic sides for the one dimensional assumption. The one-dimensional semi-infinite model is identical to the one-dimensional adiabatic side model if the source in uniform in space at any instant in time. Region 2 is now formulated as a distributed (D) system possessing a spatially and temporally varying temperature profile. In this case, thermal contact resistance is present at the interface of the two dissimilar materials at $x = L_1$. Fig. 2a provides an exploded view of a Lumped-Distributed (L-D) formulation based on the defined CV's. Fig. 2b displays a Distributed-Distributed (D-D) formulation based on the defined CV's shown in this figure. Fig. 2b displays a schematic for developing a distributed formulation for Region 1 that is connected to a distributed formulation in Region

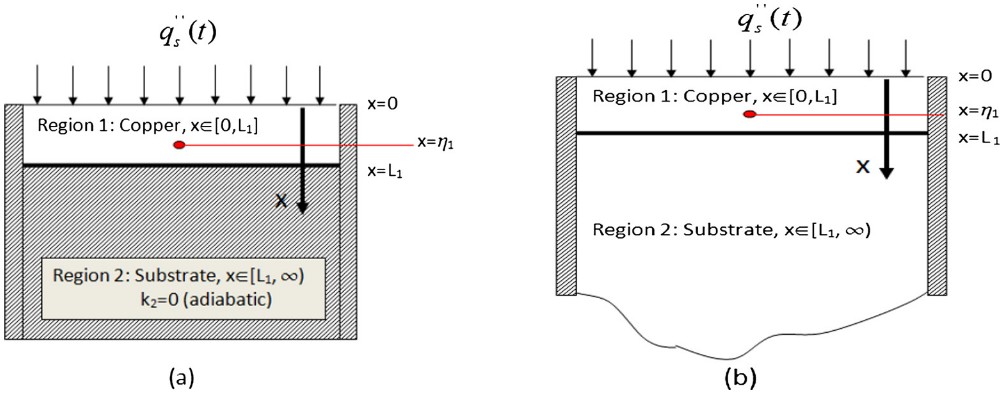

Fig. 1. Schematic of (a) idealized sensor; and (b) simplified model with adiabatic sides.

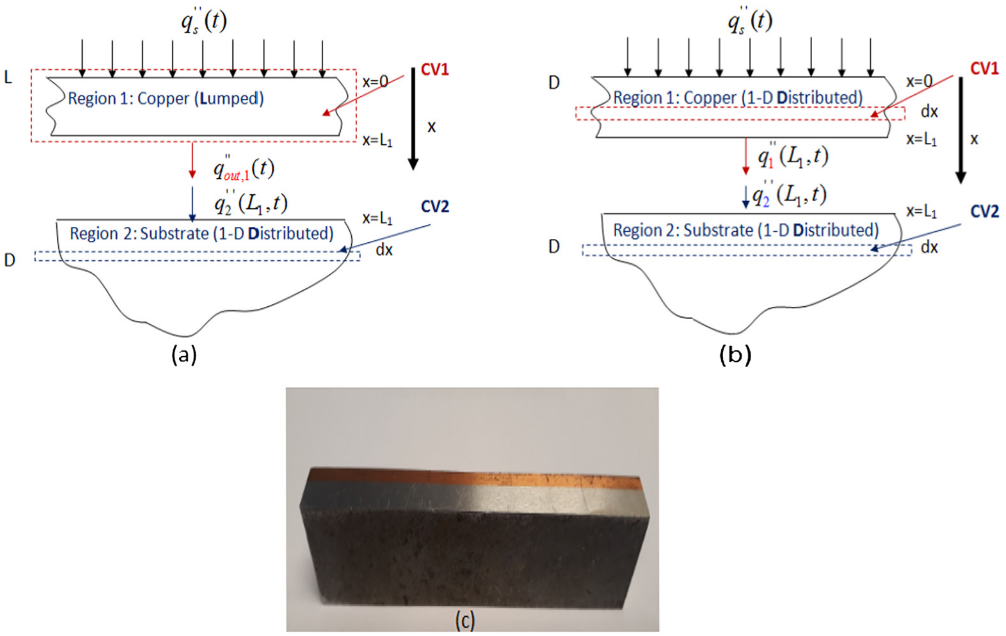

Fig. 2. Exploded view for (a) the L-D formulation; (b) the D-D formulation; and, (c) photograph of a cold-welded, two-layer sample.

2. The present study is based on the geometry provided in Fig. 2a. In this study, the onus is placed on developing an inclusive model leading to a simplified design process. Further, the mathematical formalism is based on resolving an ill-posed, first-kind Volterra integral equation. To repeat, this approach places the burden of work on the analysis process rather than the sensor's design and fabrication process. Fig. 2c displays an "explosively-welded" laminated material composed of pure copper and stainless steel (e.g. [22]). This cold-weld process produces excellent thermal contact involving a substrate material that can be easily instrumented. This process does not appear to disturb the morphology at the interface [22]. The reader is referred to Ref. 22 for further details on morphology and contact. Common practice (for non-cooled gauge) uses an insulating material as the second layer where perfect thermal contact is not assured over repeated cycling. As will be demonstrated in an upcoming study, insulation can be placed behind an instrumented substrate causing no difficulties in the analysis. In this case, second temperature probe would be installed at $x = \eta_2$, $L_1 < x < \eta_2$. The resulting data reduction equation would be derived based on the physical region, $0 \le x \le \eta_2$.

In developing the data reduction equation for this study, Region 1 is assumed to contain temperature dependent thermophysical properties while the Region 2 is assumed to possess constant thermophysical properties. This represents the first step in our proposed design process. Let the specific heat, $\widehat{c}_1(T_1^*) > 0$ for Region 1 be given as $\widehat{c}_1(T_1^*) = c_{1,0} + c_{1,1}(T_1^* - T_r)$ where T_r is a reference temperature. This temperature variation is sufficient for both demonstrating the analysis and is physically representative of copper. The initial condition is given as T_o for both regions. The reduced temperature is defined as $\theta_j = T_j - T_o$, $j = 1, 2$ which is valid for either lumped, T_j or distributed temperatures, T_j^*, $j = 1, 2$. Thus, the specific heat in Region 1 is expressed as $\widehat{c}_1(T_1^*) = c_{1,0}' + c_{1,1}(T_1^* - T_o) = c_{1,0}' + c_{1,1}\theta_1^* = c_1(\theta_1^*)$ where $c_{1,0}' = c_{1,0} + c_{1,1}(T_o - T_r)$. The specific heat for Region 2 is designated as c_2 (evaluated at the initial condition). Further, the net surface heat flux, $q''(0, t)$ is assumed to be equal to the source heat flux, $q_s''(t)$. This is a valid approximation when the source is the dominant mode of heat transfer. This approximation is often the case in aerospace ground testing. All energy balances are derived based on energy conservation given as [8,9]

$$\dot{E}_{in} + \dot{E}_{gen} = \dot{E}_{out} + \dot{E}_{stor}. \tag{1}$$

Region 1: Energy Balance

The lumped heat equation for Region 1 can be derived via a physical or mathematical formulation. The physical formulation follows the control volume, CV1 defined in Fig. 2a leading to

$$q_s''(t)A = \rho_1 \widehat{c}_1(T_1(t))L_1 A\frac{dT_1}{dt}(t) + q''_{1,out}(t)A, \quad x \in [0, L_1], \quad t \geq 0, \tag{2a}$$

or upon dividing by the cross-sectional area, A and making use of the reduced temperature definition, we get

$$q_s''(t) = \rho_1 c_1(\theta_1(t))L_1\frac{d\theta_1}{dt}(t) + q''_{1,out}(t), \quad x \in [0, L_1], \quad t \geq 0. \tag{2b}$$

It is clear, from this physical formulation, that the reduced lumped temperature, $\theta_1(t) = T_1(t) - T_o$ is solely a function of time, t and uniform in space. This temperature is not actually measureable. To illustrate the physical meaning of this temperature, we return to Eq. (1) and derive the fully-distributed, one-dimensional conservation of energy statement as [8,9]

$$\rho_1 \widehat{c}_1(T_1^*(x,t))\frac{\partial T_1^*}{\partial t}(x,t) = -\frac{\partial q_1^{*\prime\prime}}{\partial x}(x,t), \quad x \in [0, L_1], \quad t \geq 0, \tag{3a}$$

where the “astrid” superscript refers to the fully distributed formulation in Region 1. Further, Eq. (3a) in the reduced temperature variable becomes

$$\rho_1 c_1(\theta_1^*(x,t))\frac{\partial \theta_1^*}{\partial t}(x,t) = -\frac{\partial q_1^{*\prime\prime}}{\partial x}(x,t), \quad x \in [0, L_1], \quad t \geq 0. \tag{3b}$$

Assuming ρ_1 is a constant, we next integrate Eq. (3b) over the spatial variable defined by Region 1 to obtain

$$\rho_1 \int_{x=0}^{L_1} c_1(\theta_1^*)\frac{\partial \theta_1^*}{\partial t}(x,t)dx = -\int_{x=0}^{L_1} \frac{\partial q_1^{*\prime\prime}}{\partial x}(x,t)dx, \quad t \geq 0,$$

or

$$\rho_1 \int_{x=0}^{L_1} c_1(\theta_1^*)\frac{\partial \theta_1^*}{\partial t}(x,t)dx = -(q_1^{*\prime\prime}(L_1,t) - q_1^{*\prime\prime}(0,t)), \quad t \geq 0, \tag{3c}$$

which by the weighted mean-value theorem [23] produces

$$\rho_1 c_1(\theta_1^*(\xi(t),t)) \int_{x=0}^{L_1} \frac{\partial \theta_1^*}{\partial t}(x,t)dx = -(q_1^{*\prime\prime}(L_1,t) - q_1^{*\prime\prime}(0,t)), \quad t \geq 0, \tag{3d}$$

where $\xi(t) \in [0, L_1]$, $t \geq 0$ and $c_1(\theta_1^*) > 0$. Further, we can now extract the time derivative from the integrand via Leibniz rule [23] as

$$\rho_1 c_1(\theta_1^*(\xi(t),t))L_1 \frac{d}{dt}\left(\frac{\int_{x=0}^{L_1}\theta_1^*(x,t)dx}{L_1}\right) = q_s''(t) - q_1^{*\prime\prime}(L_1,t), \quad t \geq 0, \tag{3e}$$

where $q_1^*(0,t) = q_s''(t)$, $t \geq 0$. The final form becomes

$$q_s''(t) = \rho_1 c_1(\theta_1^*(\xi(t),t))L_1 \frac{d\bar{\theta}_1^*}{dt}(t) + q_1^{*\prime\prime}(L_1,t), \quad t \geq 0, \tag{4a}$$

where the average reduced temperature, $\bar{\theta}_1^*(t)$ is defined mathematically as

$$\bar{\theta}_1^*(t) = \frac{\int_{x=0}^{L_1}\theta_1^*(x,t)dx}{L_1}.$$

Equation (4a) is subject to the consistent, reduced temperature initial condition

$$\theta_1^*(\xi(0),0) = \bar{\theta}_1^*(0) = \theta_1^*(L_1,0) = 0. \tag{4b}$$

It is evident that Eq. (2b) and Eq. (4a) are mathematically similar but not identical.

Region 2: Distributed Semi-Infinite Heat Equation

For this first study, Region 2 assumes constant thermophysical properties. The heat equation for this region, in terms of the reduced temperature, $\theta_2^*(x,t)$, is [8,9]

$$\frac{1}{\alpha_2}\frac{\partial \theta_2^*}{\partial t}(x,t) = \frac{\partial^2 \theta_2^*}{\partial x^2}(x,t), \quad x \in [L_1, \infty), \quad t \geq 0, \tag{5a}$$

subject to the imposed boundary conditions

$$-k_2 \frac{\partial \theta_2^*}{\partial x}(L_1, t) = q_2^{*''}(L_1, t) = q_1^{*''}(L_1, t), \tag{5b}$$

$$\theta_2^*(L_1, t) = \theta_1^*(L_1, t), \tag{5c}$$

and far-field condition

$$\lim_{x \to \infty} \theta_2^*(x, t) = 0, \quad t > 0, \tag{5d}$$

with the initial condition

$$\theta_2^*(x, 0) = 0, \quad x \in [L_1, \infty). \tag{5e}$$

Equation (5c) expresses perfect thermal contact which, in reality, is difficult to achieve or quantify. The semi-infinite model (no thermal penetration to the back of the substrate) lends itself to the reduced Region 2 temperature-heat flux relationship at $x = L_1$ [8,24]

$$\theta_2^*(L_1, t) = \frac{1}{\beta_2 \sqrt{\pi}} \int_{u=0}^{t} \frac{q_2^{*''}(L_1, u)}{\sqrt{t-u}} du, \quad t \geq 0, \tag{6a}$$

where $\beta_2 = \sqrt{\rho_2 c_2 k_2}$ is known as the thermal product or thermal effusivity. Using the interfacial boundary conditions, Eqs. (5b-c), Eq. (6a) can be alternatively written as

$$\theta_1^*(L_1, t) = \frac{1}{\beta_2 \sqrt{\pi}} \int_{u=0}^{t} \frac{q_1^{*''}(L_1, u)}{\sqrt{t-u}} du, \quad t \geq 0. \tag{6b}$$

Next, we invert Eq. (6b) using the Abel inversion [24,25] to produce

$$q_1^{*''}(L_1, t) = \frac{\beta_2}{\sqrt{\pi}} \int_{u=0}^{t} \frac{\partial \theta_1^*}{\partial u}(L_1, u) \frac{du}{\sqrt{t-u}}, \quad t \geq 0. \tag{6c}$$

Substituting Eq. (6c) into Eq. (4a) yields

$$q_s''(t) = \rho_1 c_1(\theta_1^*(\xi(t), t)) L_1 \frac{d\bar{\theta}_1^*}{dt}(t) + \frac{\beta_2}{\sqrt{\pi}} \int_{u=0}^{t} \frac{\partial \theta_1^*}{\partial u}(L_1, u) \frac{du}{\sqrt{t-u}}, \quad t \geq 0. \tag{6d}$$

At this juncture, we now make an approximation involving the temperature variables; namely, we assume $\theta_1^*(\xi(t), t) \approx \bar{\theta}_1(t)$; $\theta_1^*(L_1, t) \approx \bar{\theta}_1(t)$; and, $\bar{\theta}_1^*(t) \approx \bar{\theta}_1(t)$. With this, Eq. (6d) becomes

$$q_s''(t) \approx \rho_1 L_1 c_1(\bar{\theta}_1(t)) \frac{d\bar{\theta}_1}{dt}(t) + \frac{\beta_2}{\sqrt{\pi}} \int_{u=0}^{t} \frac{d\bar{\theta}_1}{du}(u) \frac{du}{\sqrt{t-u}}, \quad t \geq 0, \tag{6e}$$

or

$$\underline{q}_s''(t) = \rho_1 L_1 c_1(\bar{\theta}_1(t)) \frac{d\bar{\theta}_1}{dt}(t) + \frac{\beta_2}{\sqrt{\pi}} \int_{u=0}^{t} \frac{d\bar{\theta}_1}{du}(u) \frac{du}{\sqrt{t-u}}, \quad t \geq 0, \tag{6f}$$

where $\underline{q}_s''(t) \approx q_s''(t)$, $t > 0$. The data reduction model equation is now based on Eq. (6f) with its intrinsic assumptions and proposed definition of reduced temperature. This first approximation begins the string of approximation events.

Frequency Domain Analysis for Producing a Resolvable Data Reduction Equation

Substituting the estimated specific heat, given as $c_1(\bar{\theta}_1(t)) = c'_{1,0} + c_{1,1}\bar{\theta}_1(t)$, for Region 1 into Eq. (6f) and then taking the Laplace transform yields

$$\mathcal{L}\{\underline{q}_s''(t)\} = \rho_1 L_1 \mathcal{L}\{\frac{d}{dt}\left((c'_{1,0}\bar{\theta}_1(t) + \frac{c_{1,1}}{2}\bar{\theta}_1^2(t)\right)\} + \mathcal{L}\{\frac{\beta_2}{\sqrt{\pi}} \int_{u=0}^{t} \frac{d\bar{\theta}_1}{du}(u) \frac{du}{\sqrt{t-u}}\}, \quad Re(s) \geq 0, \tag{7a}$$

where s is a complex variable with the Laplace transform being defined as [25]

$$\mathcal{L}\{f(t)\} = \hat{f}(s) = \int_{t=0}^{\infty} f(t) e^{-st} dt, \quad Re(s) > 0. \tag{7b}$$

Equation (7a) reduces to

$$\hat{\underline{q}}_s''(s) = \rho_1 L_1 s\big(c'_{1,0}\hat{\bar{\theta}}_1(s) + \frac{c_{1,1}}{2}\hat{\psi}_1(s)\big) + \beta_2 \sqrt{s}\hat{\bar{\theta}}_1(s), \quad Re(s) > 0, \tag{8a}$$

where

$$\hat{\psi}_1(s) = \mathcal{L}\{\bar{\theta}_1^2(t)\}, \quad Re(s) > 0, \tag{8b}$$

since $\psi_1(t) = \bar{\theta}_1^2(t)$, $t \geq 0$.

Equation (8a) can be expressed as

$$\hat{\underline{q}}_s''(s) = \rho_1 L_1 c_{1,0}' \hat{\bar{\theta}}_1(s)\sqrt{s}(a+\sqrt{s}) + \rho_1 L_1 \frac{c_{1,1}}{2} s\hat{\psi}_1(s), \quad Re(s) > 0, \tag{9}$$

where $a = \beta_2/(\rho_1 L_1 c_{1,0}')$. Next, dividing Eq. (9) by $\sqrt{s}(a+\sqrt{s})\rho_1 L_1 c_{1,0}'$ yields

$$\frac{1}{\rho_1 L_1 c_{1,0}'} \frac{\hat{\underline{q}}_s''(s)}{\sqrt{s}(a+\sqrt{s})} = \hat{\bar{\theta}}_1(s) + \frac{c_{1,1}}{2c_{1,0}'} \frac{\sqrt{s}}{(a+\sqrt{s})} \hat{\psi}_1(s), \quad Re(s) > 0. \tag{10a}$$

Let $b = 1/(\rho_1 L_1 c_{1,0}')$ and $r = c_{1,1}/(2c_{1,0}')$ and divide Eq. (10a) by the preconditioner, s^m, $m = 1, 2, \ldots$ to get

$$b \frac{\hat{\underline{q}}_s''(s)}{s^{m+1/2}(a+\sqrt{s})} = \frac{\hat{\bar{\theta}}_1(s)}{s^m} + r \frac{1}{s^{m-1/2}(a+\sqrt{s})} \hat{\psi}_1(s), \quad Re(s) > 0. \tag{10b}$$

Assuming a minimal regularity condition on $\hat{\psi}_1(s)$ and the availability of an analytical inversion, suggests letting $m = 1$ and thus Eq. (10b) becomes

$$b \frac{\hat{\underline{q}}_s''(s)}{s^{3/2}(a+\sqrt{s})} = \frac{\hat{\bar{\theta}}_1(s)}{s} + r \frac{1}{\sqrt{s}(a+\sqrt{s})} \hat{\psi}_1(s), \quad Re(s) > 0. \tag{10c}$$

Equation (10c) is now the data reduction equation of interest in the frequency domain. Next, let us invert Eq. (10c) using the convolution theorem [26]

$$\mathcal{L}\{\int_{u=0}^{\infty} f(u)g(t-u)du\} = \hat{f}(s) * \hat{g}(s), \quad Re(s) > 0. \tag{11}$$

Inverting Eq. (10c) produces

$$b \int_{u=0}^{t} \underline{q}_s''(u)\kappa_q(t-u)du = \int_{u=0}^{t} \bar{\theta}_1(u)du + r \int_{u=0}^{t} \bar{\theta}_1^2(u)\kappa_\psi(t-u)du, \quad t \geq 0, \tag{12a}$$

since $\psi_1(t) = \bar{\theta}_1^2(t)$ and where the kernels $\kappa_q(t)$ and $\kappa_\psi(t)$ are defined as

$$\kappa_q(t) = \mathcal{L}^{-1}\{\frac{1}{s^{3/2}(a+\sqrt{s})}\} = \frac{1}{a^2}\left(\frac{2a\sqrt{t}}{\sqrt{\pi}} - 1 + e^{a^2 t} erfc(a\sqrt{t})\right), \tag{12b}$$

$$\kappa_\psi(t) = \mathcal{L}^{-1}\{\frac{1}{\sqrt{s}(a+\sqrt{s})}\} = e^{a^2 t} erfc(a\sqrt{t}), \quad t \geq 0, \tag{12c}$$

where $erfc(z)$ is the complementary error function. Observe that all auxiliary conditions are absorbed into the integral representation. Equation (12a) is a linear, first-kind Volterra integral equation for the unknown surface heat flux, $\underline{q}_s''(t) \approx q_s''(t)$, $t \geq 0$.

Next, let us assume that "measured" instrument temperature, $\theta_{\eta_1}(t)$ is equal to the "exact" positional temperature, $\theta_1^*(\eta_1, t)$ where $\eta_1 \in [0, L_1]$ per Fig. 1b, i.e. $\theta_{\eta_1}(t) = \theta_1^*(\eta_1, t)$. At this point, perfect reduced temperature measurements are assumed in this derivation. Next, we assume that the average temperature, $\bar{\theta}_1(t)$ is equal to the measured positional temperature, $\theta_1^*(\eta_1, t)$. Equation (12a) is now expressed as

$$b \int_{u=0}^{t} \underline{q}_s''(u)\kappa_q(t-u)du \approx \int_{u=0}^{t} \theta_1^*(\eta_1, u)du + r \int_{u=0}^{t} \left(\theta_1^*(\eta_1, u)\right)^2 \kappa_\psi(t-u)du, \quad t \geq 0, \tag{13a}$$

or

$$b \int_{u=0}^{t} \underline{q}_{s,\eta_1}''(u)\kappa_q(t-u)du = \int_{u=0}^{t} \theta_1^*(\eta_1, u)du + r \int_{u=0}^{t} \left(\theta_1^*(\eta_1, u)\right)^2 \kappa_\psi(t-u)du, \quad t \geq 0, \tag{13b}$$

which now extends the approximation thread to $q_s''(t) \approx \underline{q}_s''(t) \approx \underline{q}_{s,\eta_1}''(t)$.

It should be remarked that prefiltering the data disrupts the equal sign in Eq. (6f) even in the presence of ideal data. In contrast, the preconditioner operates on the equation itself thereby preserving the equal sign even in the presence of ideal data. Hence, as this is an ill-posed problem that is highly sensitive to noise, the concept of preconditioning the functional equation describing the energy balance is preferred.

3. Regularization and numerical methods

This section provides the final computational form of the data reduction equation for recovering an approximation of $q_s''(t)$ in a discrete sense where the reduced temperature data are imperfect. Numerical results, for the heat flux, require stabilization owing to the ill-posed nature of the formulation. In this context, the notion of future-time is introduced for accomplishing the regularization. Regularization is a means for introducing filtering. This approach basically transforms the first-kind integral equation for the heat flux into an approximate second-kind Volterra integral equation. This new equation possesses stronger stability characteristics than the original first-kind form. For additional insight, the reader is referred to Refs. [17,18,27]. In a nutshell, time is advanced by $t \to t+\gamma$ with $\gamma \geq 0$ where γ is the future-time parameter (or regularization parameter). As written, γ forms a continuous spectrum of values. Substituting this time advancement into Eq. (13b) produces

$$b \int_{u=0}^{t+\gamma} \underline{q}''_{s,\eta_1}(u)\kappa_q(t+\gamma-u)du = \int_{u=0}^{t+\gamma} \theta_1^*(\eta_1,u)du + r \int_{u=0}^{t+\gamma} \left(\theta_1^*(\eta_1,u)\right)^2 \kappa_\psi(t+\gamma-u)du, \quad t \geq 0, \tag{14a}$$

or

$$\begin{aligned} & b \int_{u=0}^{t} \underline{q}''_{s,\eta_1}(u)\kappa_q(t+\gamma-u)du + b \int_{u=t}^{t+\gamma} \underline{q}''_{s,\eta_1}(u)\kappa_q(t+\gamma-u)du \\ & \quad = \int_{u=0}^{t+\gamma} \theta_1^*(\eta_1,u)du + r \int_{u=0}^{t+\gamma} \left(\theta_1^*(\eta_1,u)\right)^2 \kappa_\psi(t+\gamma-u)du, \quad t \geq 0, \end{aligned} \tag{14b}$$

or

$$\begin{aligned} & b \int_{u=0}^{t} \underline{q}''_{s,\eta_1}(u)\kappa_q(t+\gamma-u)du + b\underline{q}''_{s,\eta_1}(t) \int_{u=t}^{t+\gamma} \kappa_q(t+\gamma-u)du \\ & \quad \approx \int_{u=0}^{t+\gamma} \theta_1^*(\eta_1,u)du + r \int_{u=0}^{t+\gamma} \left(\theta_1^*(\eta_1,u)\right)^2 \kappa_\psi(t+\gamma-u)du, \quad t \geq 0, \end{aligned} \tag{14c}$$

where we assume $\underline{q}''_{s,\eta_1}(u) \approx \underline{q}''_{s,\eta_1}(t)$, in $u \in [t, t+\gamma]$. Recovering the equal sign suggests

$$\begin{aligned} & b \int_{u=0}^{t} \underline{q}''_{s,\eta_1,\gamma}(u)\kappa_q(t+\gamma-u)du + bC_\gamma \underline{q}''_{s,\eta_1,\gamma}(t) \\ & \quad = \int_{u=0}^{t+\gamma} \theta_1^*(\eta_1,u)du + r \int_{u=0}^{t+\gamma} \left(\theta_1^*(\eta_1,u)\right)^2 \kappa_\psi(t+\gamma-u)du, \quad t \geq 0, \end{aligned} \tag{14d}$$

where

$$C_\gamma = \int_{u=t}^{t+\gamma} \kappa_q(t+\gamma-u)du = \int_{z=0}^{\gamma} \kappa_q(z)dz, \quad \gamma \geq 0, \tag{14e}$$

which now extends the approximation thread to $q_s''(t) \approx \underline{q}_s''(t) \approx \underline{q}''_{s,\eta_1}(t) \approx \underline{q}''_{s,\eta_1,\gamma}(t)$. At this juncture, it is prudent to move from the continuous domain into the discrete domain as expected when experimental data are available. Let the time sample spacing be defined as $\Delta t = t_{max}/N$ where N data points exist beyond the initial condition. The time span of the experiment is denoted as t_{max}. The sampling frequency is $f_s = 1/\Delta t$. It is also convenient to move the defined continuous parameter, γ into its discrete counterpart defined as $\gamma_m = mM_f \Delta t$, $m = 1, 2, ..., P$ and where M_f is a convenient multiplication factor. For numerical convenience, observe that γ_m is defined in terms of sampling frequency. Therefore, letting $t \to t_i$ and $\gamma \to \gamma_m$ in Eq. (14d) produces

$$\begin{aligned} & b \int_{u=0}^{t_i} \underline{q}''_{s,\eta_1,\gamma_m}(u)\kappa_q(t_i+\gamma_m-u)du + bC_{\gamma_m} \underline{q}''_{s,\eta_1,\gamma_m}(t_i) \\ & \quad = \int_{u=0}^{t_i+\gamma_m} \theta_1^*(\eta_1,u)du + r \int_{u=0}^{t_i+\gamma_m} \left(\theta_1^*(\eta_1,u)\right)^2 \kappa_\psi(t_i+\gamma_m-u)du, \quad i = 1, 2, ..., N - mM_f, \end{aligned} \tag{15a}$$

while Eq. (14e) becomes

$$C_{\gamma_m}=\int\limits_{z=0}^{\gamma_m}\kappa_q(z)dz,\quad m=1,2,...,P. \tag{15b}$$

Observe that the resolvable heat flux prediction is reduced to $t'_{max}=t_{max}-\gamma_m$ or $(N-mM_f)\Delta t$. Next, we subdivide the integration regions per data panel as

$$\begin{aligned}&b\sum_{j=1}^{i}\int\limits_{u=t_{j-1}}^{t_j}\underline{q}''_{s,\eta_1,\gamma_m}(u)\kappa_q(t_i+\gamma_m-u)du+bC_{\gamma_m}\underline{q}''_{s,\eta_1,\gamma_m}(t_i)\\&=\sum_{j=1}^{i+mM_f}\int\limits_{u=t_{j-1}}^{t_j}\theta_1^*(\eta_1,u)du+r\sum_{j=1}^{i+mM_f}\int\limits_{u=t_{j-1}}^{t_j}\left(\theta_1^*(\eta_1,u)\right)^2\kappa_\psi(t_i+\gamma_m-u)du,\quad i=1,2,...,N-mM_f;m=1,2,...,P.\end{aligned} \tag{16a}$$

Generalized product integration [24] is now introduced through

$$\begin{aligned}&b\sum_{j=1}^{i}\underline{q}''_{s,\eta_1,\gamma_m}(t_j)\int\limits_{u=t_{j-1}}^{t_j}\kappa_q(t_i+\gamma_m-u)du+bC_{\gamma_m}\underline{q}''_{s,\eta_1,\gamma_m}(t_i)\\&\approx\sum_{j=1}^{i+mM_f}\theta_1^*(\eta_1,t_j)\int\limits_{u=t_{j-1}}^{t_j}du+r\sum_{j=1}^{i+mM_f}\left(\theta_1^*(\eta_1,t_j)\right)^2\int\limits_{u=t_{j-1}}^{t_j}\kappa_\psi(t_i+\gamma_m-u)du,\quad i=1,2,...,N-mM_f;m=1,2,...,P,\end{aligned} \tag{16b}$$

or in order to recover the equal sign, we write

$$\begin{aligned}&b\sum_{j=1}^{i}\underline{q}''_{s,\eta_1,\gamma_m,N}(t_j)M_q(j,i,m)+bC_{\gamma_m}\underline{q}''_{s,\eta_1,\gamma_m,N}(t_i)\\&=\Delta t\sum_{j=1}^{i+mM_f}\theta_1^*(\eta_1,t_j)+r\sum_{j=1}^{i+mM_f}\left(\theta_1^*(\eta_1,t_j)\right)^2M_\psi(j,i,m),\quad i=1,2,...,N-mM_f;m=1,2,...,P,\end{aligned} \tag{16c}$$

$$M_q(j,i,m)=\int\limits_{u=t_{j-1}}^{t_j}\kappa_q(t_i+\gamma_m-u)du,\quad j=1,2,...,i, \tag{16d}$$

$$M_\psi(j,i,m)=\int\limits_{u=t_{j-1}}^{t_j}\kappa_\psi(t_i+\gamma_m-u)du,\quad j=1,2,...,i+mM_f;i=1,2,...,N-mM_f;m=1,2,...,P, \tag{16e}$$

which now extends the approximation thread to $q''_s(t)\approx\underline{q}''_s(t)\approx\underline{q}''_{s,\eta_1}(t)\approx\underline{q}''_{s,\eta_1,\gamma_m}(t)\approx\underline{q}''_{s,\eta_1,\gamma_m,N}(t)$. Equations (16d,e) can either be analytically or numerically integrated. It is evident that an explicit expression for the heat flux, $\underline{q}''_{s,\eta_1,\gamma_m,N}(t_i)$ avails itself with one more manipulation. Releasing $j=i$ in the first summation on the left-hand side of Eq. (16c) and solving for the heat flux, $\underline{q}''_{s,\eta_1,\gamma_m,N}(t_i)$ renders

$$\underline{q}''_{s,\eta_1,\gamma_m,N}(t_i)=\frac{\Delta t\sum_{j=1}^{i+mM_f}\theta_1^*(\eta_1,t_j)+r\sum_{j=1}^{i+mM_f}\left(\theta_1^*(\eta_1,t_j)\right)^2M_\psi(j,i,m)-b\sum_{j=1}^{i-1}\underline{q}''_{s,\eta_1,\gamma_m,N}(t_j)M_q(j,i,m)}{bM_q(i,i,m)+bC_{\gamma_m}}, \tag{17}$$

$i=1,2,...,N-mM_f$; $m=1,2,...,P$. As with all experimental studies, the measured data are inexact, that is, $\theta_1^*(\eta_1,t_i)\approx\tilde{\theta}_1^*(\eta_1,t_i)$, $i=1,2,...,N$ which when substituted into Eq. (17) produces

$$\underline{q}''_{s,\eta_1,\gamma_m,N}(t_i)\approx\frac{\Delta t\sum_{j=1}^{i+mM_f}\tilde{\theta}_1^*(\eta_1,t_j)+r\sum_{j=1}^{i+mM_f}\left(\tilde{\theta}_1^*(\eta_1,t_j)\right)^2M_\psi(j,i,m)-b\sum_{j=1}^{i-1}\underline{q}''_{s,\eta_1,\gamma_m,N}(t_j)M_q(j,i,m)}{bM_q(i,i,m)+bC_{\gamma_m}}, \tag{18a}$$

$i=1,2,...,N-mM_f$; $m=1,2,...,P$ or

$$\tilde{\underline{q}}''_{s,\eta_1,\gamma_m,N}(t_i)=\frac{\Delta t\sum_{j=1}^{i+mM_f}\tilde{\theta}_1^*(\eta_1,t_j)+r\sum_{j=1}^{i+mM_f}\left(\tilde{\theta}_1^*(\eta_1,t_j)\right)^2M_\psi(j,i,m)-b\sum_{j=1}^{i-1}\tilde{\underline{q}}''_{s,\eta_1,\gamma_m,N}(t_j)M_q(j,i,m)}{bM_q(i,i,m)+bC_{\gamma_m}}, \tag{18b}$$

$i=1,2,...,N-mM_f$; $m=1,2,...,P$ which now extends the approximation thread to $q''_s(t)\approx\underline{q}''_s(t)\approx\underline{q}''_{s,\eta_1}(t)\approx\underline{q}''_{s,\eta_1,\gamma_m}(t)\approx\underline{q}''_{s,\eta_1,\gamma_m,N}(t)\approx\tilde{\underline{q}}''_{s,\eta_1,\gamma_m,N}(t)$. It is clear that experimental data reduction introduces an approximation thread into the interpretation process. As with all ill-posed problems, the key element lies in the prediction of the optimal regularization parameter, γ_{opt}. Too small a value leads to instabilities while too large a value leads to oversmoothing. Preconditioning assists in defining a means for acquiring the optimal regularization parameter using the proposed methods to be described in Section 4.

Table 1
Simulation parameters.

Parameter/Property	Value	Units
$k_{1,0}$	405	W/(m-K)
$k_{1,1}$	-0.0619	W/(m-K^2)
$k_{2,0}$	14.5	W/(m-K)
$k_{2,1}$	0.0151	W/(m-K^2)
$c_{1,0}$	385	J/(kg-K)
$c_{1,1}$	0.0967	J/(kg-K^2)
$c_{2,0}$	470	J/(kg-K)
$c_{2,1}$	0.1930	J/(kg-K^2)
ρ_1	8750	kg/m^3
ρ_2	7920	kg/m^3
t_{max}	14	s
N	700	–
Δt	0.02	s
f_s	50	Hz
T_{ref}	273.15	K
T_o	293.15	K
q''_o	100	W/cm^2
L_1	3	mm

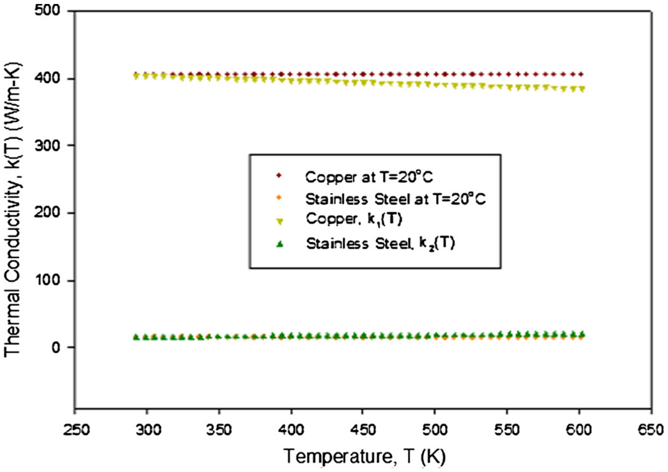

Fig. 3. Thermal conductivity as function of temperature.

4. Results

This section provides a progressive series of numerical experiments based on synthetic temperature data generated by a fixed input model using the parameters given in Table 1. That is, to emulate experimental data, a fully nonlinear distributed system is used for acquiring the temperature distribution in each region. These data are "numerically" exact to 16 places. These data are then downsampled to a physically acceptable sampling rate involving non-impulsive time scales. Table 1 provides the geometrical; and, thermophysical and mechanical properties used to generate these data. The thermophysical properties used in this study are representative values for pure copper and stainless steel 304. As this is a numerical study, these estimations are deemed appropriate. Using higher-order temperature dependencies does not cause any formulation difficulties (see Eq. (7a) and expressed conservative form). Recall, $\Psi_j(\Theta_j) = \Psi_{j0} + \Psi_{j1}(\Theta_j - \Theta_{ref})$ where Ψ can represent either thermal conductivity or specific heat while Θ can represent the regionally reduced temperature based on the input model chosen. Figs. 3 and 4 display the thermal conductivities and specific heats, respectively used in the modeling process; and, while Table 1 contains the necessary coefficients to generate Figs. 3 and 4. The source heat flux, $q''_s(t)$ for the present investigation is defined by

$$q''_s(t) = \begin{cases} 0, & 0s \le t \le 2s; \\ q''_o, & 2s < t \le 12s; \text{ and,} \\ 0, & 12s < t \le t_{max} = 14s, \end{cases}$$

where q''_o is provided in Table 1. This model suggests that the net surface flux, $q''_1(0,t)$ is zero for $t > 12s$ (which is not physically correct due to other modes of heat transfer). However, this step change is often used in the modeling process due to its severity.

Before comparing data reduction models ($r = 0$: L-D with constant specific heat in Region 1 with $r \neq 0$: L-D with temperature dependent specific heat in Region 1), let us view the input temperatures generated using a fully distributed formulation for each region based on (a) constant properties evaluated at $T_o = 293.15$ K and (b) fully temperature dependent properties (per Table 1). This is illustrated as many investigators use constant property input data sets to justify accuracy of their inverse prediction based on a constant property data

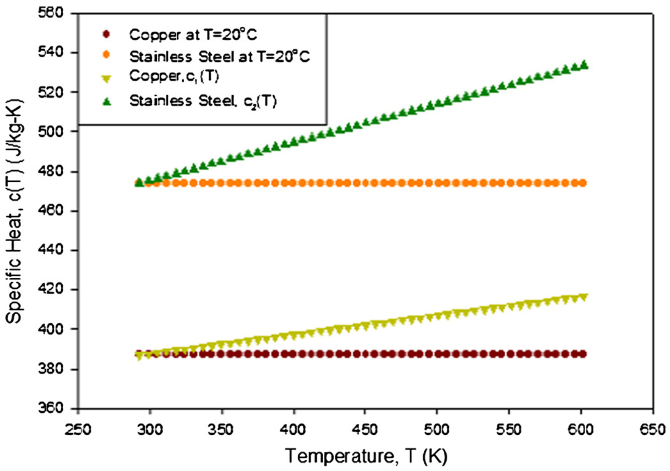

Fig. 4. Specific heat as function of temperature.

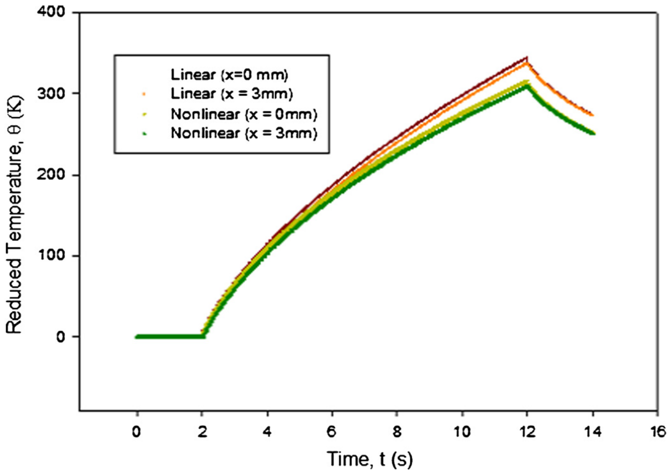

Fig. 5. Constant property and temperature dependent property input data models.

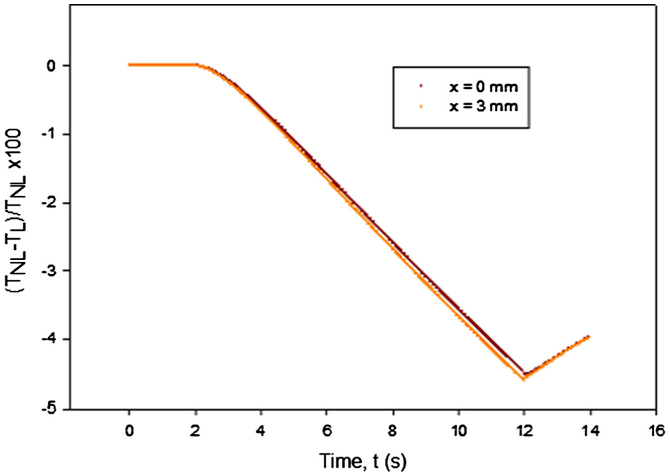

Fig. 6. Percent difference between two input models.

reduction equation. This removes the effect of real material properties unless clearly justified (e.g. low temperature rise as developed in a shock tube experiment). Fig. 5 displays the copper's reduced temperatures at $x = 0, L_1$ for the two input models. Observe that a 30 K difference occurs at the peak value. Fig. 6 provides a percent difference, as defined as, $(T_{linear} - T_{nonlinear})/T_{nonlinear} \times 100$. This figure indicates a maximum of 5% in the indicated time and temperature ranges.

Fig. 7 provides insight into the previously noted temperature drop in the copper region. This is important as the copper region is assumed lumped. Hence, the temperature drop is assumed small. As seen in Fig. 7, both input models show a relatively small temperature drop (approximately $7K$). This temperature drop across the thickness is acceptable for the lumped formulation.

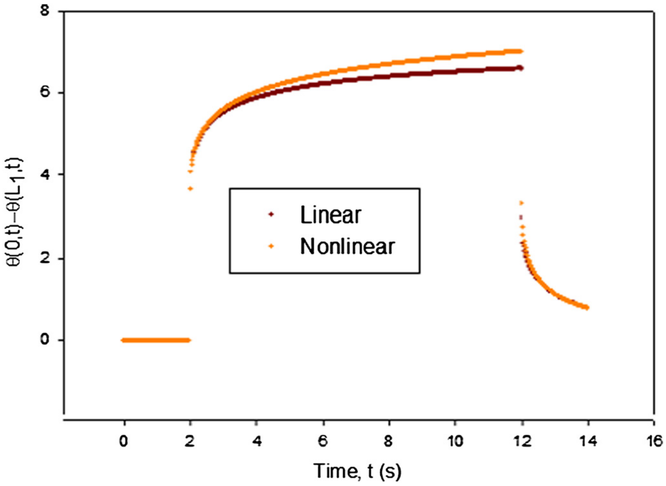

Fig. 7. Temperature drop in copper using constant and temperature dependent property input models.

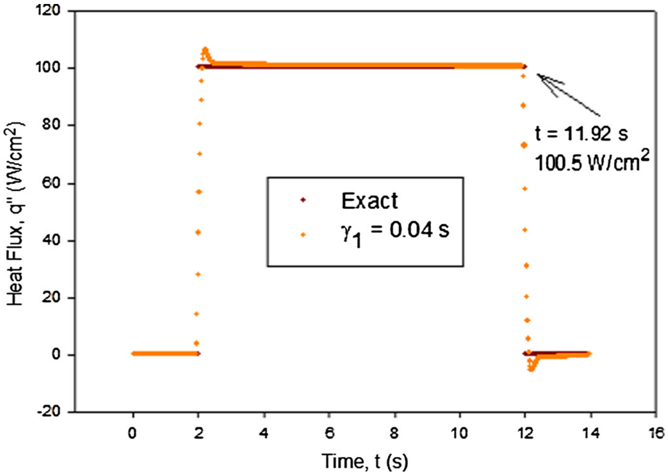

Fig. 8. Linear input model with constant property ($r = 0$) data reduction equation.

Next, let us now consider the data reduction model given in Eq. (12a) or (18b) with $r = 0$, using both input data sets; and, shortly $r \neq 0$ where the input temperatures are based on temperature dependent thermophysical properties. Again, all input data are determined from a fully distributed, one-dimensional study. The lumped temperature for Region 1 is always assumed to be the distributed temperature at $x = L_1/2$. Practically speaking, this is how the 3 mm layer will be instrumented as installing a sensor at either $x = 0$ or $x = L_1$ is not practical, possible or advisable.

Case 1: Linearized Data Reduction, $r = 0$ using constant and temperature dependent property data sets

For this initial test, the data reduction equation described in Eq. (12a) and Eq. (18b) use $r = 0$. The thermophysical properties are evaluated at the initial condition $T_o = 293.15$ K. The sampling rate is 50 Hz though similar results were obtained using 100 Hz. Fig. 8 displays the exact heat flux and the reconstructed heat flux using the L-D data reduction equation when $\gamma_1 = 0.04s$. This case indicates that estimating the lumped temperature by the probe positional temperature is highly reasonable. This makes sense in light of Fig. 7 and the physical heating scenario.

Fig. 9 presents the predicted heat flux using temperature data collected at $x = L_1/2$ as generated by the fully distributed formulation using temperature dependent thermophysical properties. This case is closer to reality. The L-D data reduction equation ($r = 0$) displays the effect of "real" data. The total temperature rise in this study is not deemed excessive but clearly shows the effect of physically "real" data. Basically, the constant property data reduction equation is now rendering about a 11% difference (or bias) at $t = 11.92s$. This time is chosen based on subtracting $2 \times \gamma_1$ for reducing the forward influencing data. This value is used as a common marker for comparison.

The heat flux predictions in these two cases are based on the future-time parameter, $\gamma_1 = 0.04s$. In the presence of ideal data, it can be shown that little future time is required for recovering the optimal heat flux prediction. Discussion on choosing the value for this parameter is held until noisy data are implemented. The heat flux "jump" case displays a notable Gibbs-like phenomena. For the present study, all numerical temperature histories are assumed to be equal to the probe temperature. This basically assumes idealized sensors. As noted earlier, in-situ thermocouples produce subtle effects due to their intrusiveness.

Case 2: Data Reduction, $r \neq 0$ using temperature dependent input model

Next, consider the data reduction equation that accounts for a temperature dependent specific heat in Region 1; namely Eq. (12a) and Eq. (18b) with $r \neq 0$. Recall that this data reduction model assumes that Region 1 is spatially lumped while possessing a temperature

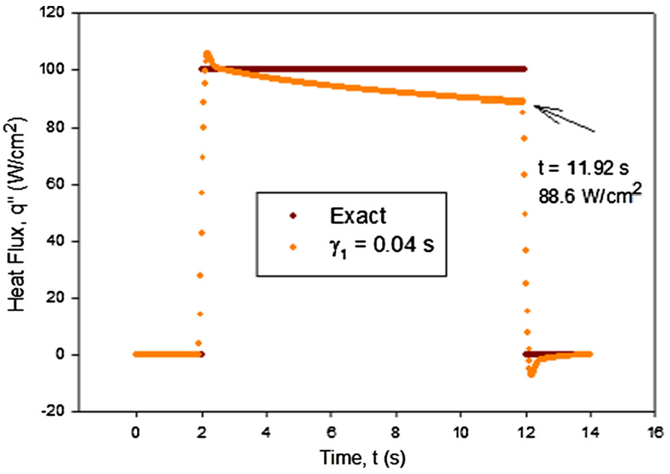

Fig. 9. Temperature dependent input model with constant property ($r = 0$) data reduction equation.

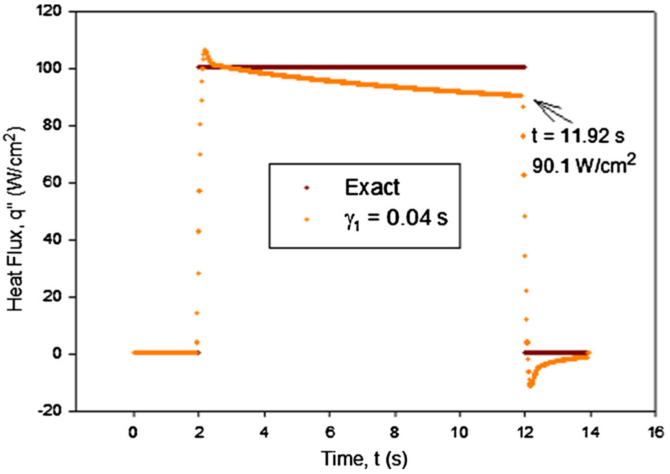

Fig. 10. Nonlinear input model for producing reduced temperature with $r \neq 0$ data reduction equation.

dependent specific heat. The stainless steel substrate assumes constant properties evaluated at the initial condition. This contrast is performed for comparing the effect constant specific heat (Fig. 9) to a more realistic temperature varying specific heat in the copper slug. Fig. 10 displays the reconstructed surface heat flux using the input data created from the fully nonlinear input model and data reduction equation with $r \neq 0$. For copper, only a small amount improvement is gained in the heat flux reconstruction. This has been similarly observed in copper-based, null-point calorimetry (using the linear heat equation). However, the present formulation can easily accommodate such variability in the presence of alternative materials. This comparison also helps establish the cause of the bias through eliminating this issue. First, this sensor design permits good interfacial contact which promotes the mathematical assumptions imposed in the analysis. Further, it is possible to bond a three-layer configuration involving copper-stainless steel-copper that can be highly useful if the calorimeter requires a backside cooling loop for highly elevated temperature cases. The copper third layer would help recover the one-dimensional assumption needed in the slug-substrate model. Second, the analytical form producing Eqs. (12a) and (18b) are computationally simple and perform well in the reconstruction under noiseless data. Third, Figs. 7–9 suggest that the substrate region model requires additional material behavior accountability in the substrate (Region 2). This can be shown by determining the heat flux leaving the fully nonlinear input model at $x = L_1$ and substituting this time-varying result into a consistent form of Eq. (2a). This identified “culprit” is the key element for adjusting the sensor's instrumention/analysis plan in order to achieve the desired high-accuracy, heat flux goal. This is the topic of the next paper. Finally, we must now address the presence of noise in the temperature data; and, demonstrate that Eq. (18b) can be used to accurately reconstruct the surface heat flux per chosen model (i.e., Fig. 10).

Case 3: Data Reduction, $r \neq 0$ using nonlinear input temperature model with noise addition at probe site

Case 3 demonstrates heat flux recoverability in the presence of noisy temperature data that are collected at the probe site, $\eta_1 = L_1/2$. This step is significant as all future formulations will be designed to produce a similar functional form, i.e., linear first-kind Volterra integral equation in surface (net) heat flux. Noisy data are generated per

$$\tilde{\theta}_1^*(\eta_1, t_j) = \theta_1^*(\eta_1, t_j) + \epsilon r_j ||\theta_1^*(\eta_1, t)||_\infty, \quad j = 1, 2, ..., N,$$

where $\eta_1 = L_1/2$, r_j is the jth random number drawn from the interval $[-1, 1]$ and ϵ is a noise factor. This is a rather extreme form of error generation but serves to illustrate the methodology. For this set of results, $\epsilon = 0.005$, leading to noise addition of $\pm 1.6K$ or $\approx 0.5\%$ error. Type T thermocouples (limited to about 350 °C) offers a similar limit of error specification [28]. Fig. 11 provides the reduced

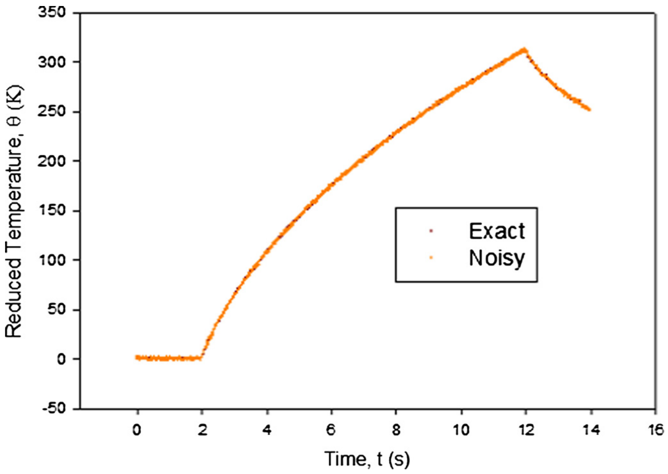

Fig. 11. Reduced temperature for exact and noisy data at the probe location.

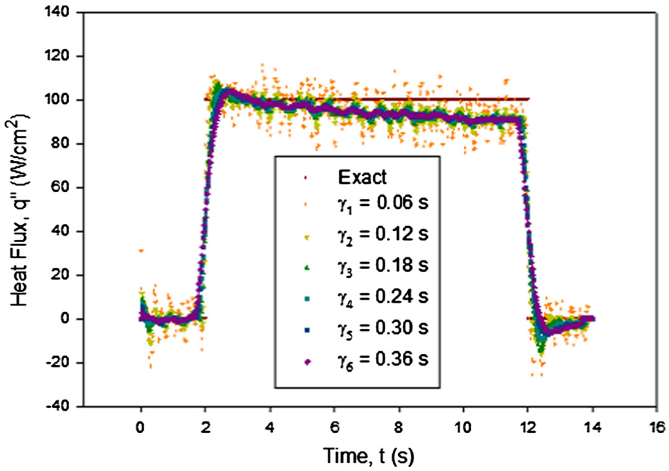

Fig. 12. Family of heat flux predictions when $r \neq 0$ in the data reduction equation.

temperature with and without noise addition at $x = \eta_1 = L_1/2$ that are downsampled to 50 Hz using the fully nonlinear forward coupled solutions for Region 1 and 2.

Fig. 12 presents a family of heat flux predictions using the regularization parameter defined by $\gamma_m = mM_f \Delta t$ where $M_f = 3$. This value of M_f is chosen in order to provide some separation between two incremental predictions. The next question arises "What is the optimal prediction and how does one extract it?". This is actually the crux of inverse problems as classical error analysis concepts are not applicable. It is observed that as γ_m increases a smoother prediction results. This occurs as less higher frequencies in the signal are retained as the regularization parameter increases. Hence, oversmoothing will occur at some point beyond the optimal value leading to error growth. Large oscillations are expected for regularization parameters smaller than the optimal value. That is, retaining too many high frequencies in the measured signal plays havoc on time differentation of the temperature data [12–14]. It should be noted that this occurs even when the formulation does not explicitly display the time derivative of temperature.

Fig. 13 displays the corresponding heat flux phase-plane ($\frac{dq''}{dt}$ vs. q'' where t is parameterized) over a family of regularized predictions [29,30]. Here, the heat flux rate, $\frac{dq''}{dt}$ is calculated by central finite differences; and forward/backward differences at the end points. In general, this figure assists in eliminating unstable predictions (too small γ_m) that retain too many high frequencies in the signal. This is seen when $m = 1$, $\gamma_1 = 0.06s$. The left grouping is clearly associated with $t \leq t_{on}$ and $t_{off} \leq t \leq t_{max} - mM_f \Delta t$ while the right grouping is associated with $t_{on} < t < t_{off}$. Bias in the data reduction model is graphically evident. Identifying the jump from instability to stability for increasing future-time parameter provides the glimpse into sufficient prediction smoothness. This is qualitatively seen between the phase plane predictions of γ_1 and γ_2. Oversmoothing is evident in the core displayed by the two groupings. At this juncture, γ_2 appears to be in proximity of the optimal regularization parameter. It should be noted that an "exact" value for γ is not necessary (or practical or potentially possible) for inverse problems.

Significant amount of insight into the estimation of the optimal regularization parameter can be obtained by a well considered experimental test run. In fact, a step heat flux source is a good place to begin. This will be discussed in a later study. In numerical studies, which are intended as a first means of discovery, the error is calculable and can provide guidance into developing a "rule" or set of "criteria" for extracting γ_{opt}. Table 2 provides some obvious metrics. Here, the heat flux root-mean-square error (RMSE) error is defined as

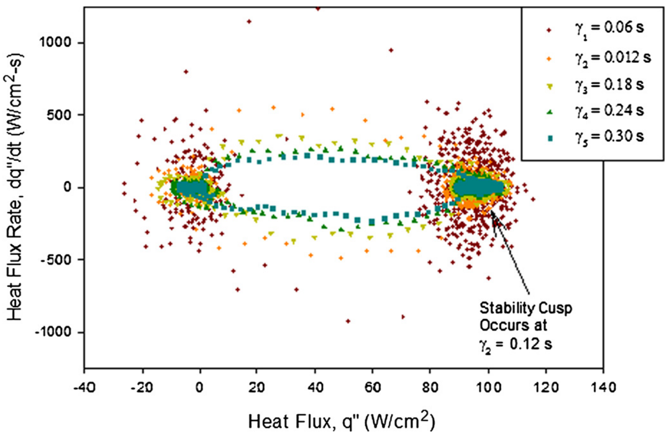

Fig. 13. Heat flux phase plane.

Table 2
Output calculations (A: $t \in [0, t'_{max}]$, B: $t \in [t_{on}, t_{off}]$).

m	γ_m (s)	$\epsilon_{q,m}$ (W/cm^2)	A: $\frac{dq''}{dt}\vert_{avg}$ (W/m^2-s)	B: $\frac{dq''}{dt}\vert_{avg}$ (W/m^2-s)
1	0.06	9.64	−11623	13328
2	**0.12**	8.16	−5144	2713
3	0.18	8.56	−4469	−1076
4	0.24	9.17	−3963	−5560
5	0.30	9.83	−3617	−5937
6	0.36	10.5	−2903	−6631
7	0.42	11.1	−2959	−7418
8	0.46	11.7	−3674	−8431
9	0.54	12.3	−4283	−9429

$$\epsilon_{q,m} = \sqrt{\sum_{j=1}^{N-mM_f} \frac{(q''_s(t_j) - \underline{\tilde{q}}''_{s,\eta_1,\gamma_m,N}(t_j))^2}{N-mM_f}}, \quad m = 1, 2, ..., P, \tag{19}$$

which, of course, is not available in experimental test campaigns. Table 2 indicates $\gamma_2 = 0.12s \approx \gamma_{opt}$. The RMSE metric may not actually be the “best” metric for ill-posed problems. From an experimental view point, the introduced step heat flux brings additional insight into both the present problem and calibration studies [30]. Reviewing, the family of heat flux predictions, indicates some data reduction model deficiency as the source is not fully reconstructed. The simplicity of the imposed heat flux indicates that the heat flux rate should be negative for all stable future-time parameters, γ_m. It is interesting to note the sudden changes in columns 4 and 5 in Table 2. In fact, the average heat flux rate (slope) from Fig. 12 indicates a negative value. Observe that the heat flux rate distinctively jumps from a positive value to a negative value in column 5 at $m = 3$ or $\gamma_3 = 0.18$ s.

Another measure that has been successful is based on cross-correlation principles [29,30] whereby one interprets “closeness” or pattern development over a parameter set. In this problem, the parameter set involves the regularization parameter, γ_m. Let the surface heat flux, cross-correlation coefficient be given as [29,30]

$$R_q(\tilde{q}''_{s,\eta_1,\gamma_m,N}, \tilde{q}''_{s,\eta_1,\gamma_{m+1},N}) = \frac{\sum_{j=0}^{N-(m+1)M_f} \tilde{q}''_{s,\eta_1,\gamma_m,N}(0,t_j)\tilde{q}''_{s,\eta_1,\gamma_{m+1},N}(0,t_j)}{\sqrt{\sum_{j=0}^{N-(m+1)M_f}(\tilde{q}''_{s,\eta_1,\gamma_m,N}(0,t_j))^2 \sum_{j=0}^{N-(m+1)M_f}(\tilde{q}''_{s,\eta_1,\gamma_{m+1},N}(0,t_j))^2}}, \tag{20a}$$

while the surface heat flux rate cross-correlation coefficient is defined as

$$R_{\dot{q}}(\dot{\tilde{q}}''_{s,\eta_1,\gamma_m,N}, \dot{\tilde{q}}''_{s,\eta_1,\gamma_{m+1},N}) = \frac{\sum_{j=0}^{N-(m+1)M_f} \dot{\tilde{q}}''_{s,\eta_1,\gamma_m,N}(0,t_j)\dot{\tilde{q}}''_{s,\eta_1,\gamma_{m+1},N}(0,t_j)}{\sqrt{\sum_{j=0}^{N-(m+1)M_f}(\dot{\tilde{q}}''_{s,\eta_1,\gamma_m,N}(0,t_j))^2 \sum_{j=0}^{N-(m+1)M_f}(\dot{\tilde{q}}''_{s,\eta_1,\gamma_{m+1},N}(0,t_j))^2}}, \tag{20b}$$

$m = 1, 2, ..., P - 1$. Let the proposed stopping criterion be given by $R_q(\tilde{q}''_{s,\eta_1,\gamma_m,N}, \tilde{q}''_{s,\eta_1,\gamma_{m+1},N}) \to 1$ and $R_{\dot{q}}(\dot{\tilde{q}}''_{s,\eta_1,\gamma_m,N}, \dot{\tilde{q}}''_{s,\eta_1,\gamma_{m+1},N}) \approx 0.75$ which correlates well with the root-mean-square error (RMSE). Of course, the RMSE is only available in simulation studies. This chosen criterion is based on simulation, estimated noise level, experiments, and experience.

For graphical simplicity in axis definitions, let $R(q'') = R_q(\tilde{q}''_{s,\eta_1,\gamma_m,N}, \tilde{q}''_{s,\eta_1,\gamma_{m+1},N})$ and $R(dq''/dt) = R_{\dot{q}}(\dot{\tilde{q}}''_{s,\eta_1,\gamma_m,N}, \dot{\tilde{q}}''_{s,\eta_1,\gamma_{m+1},N})$ in Fig. 14. Fig. 14 displays the cross-correlation phase plane. As remarked earlier, it is normally important to retain sufficient high frequencies in the signal and hence one often chooses the lower value in the pairing set. Fig. 15 presents the exact source heat flux; and, two of the “best” reconstructed surface heat fluxes using γ_2 and γ_3. Both of these results appear graphically similar. Again, the discrepancy between the predicted heat flux and exact heat flux is due to bias in the data reduction model. However, the proposed numerical procedure display robustness, stability and accuracy when compared with Fig. 10.

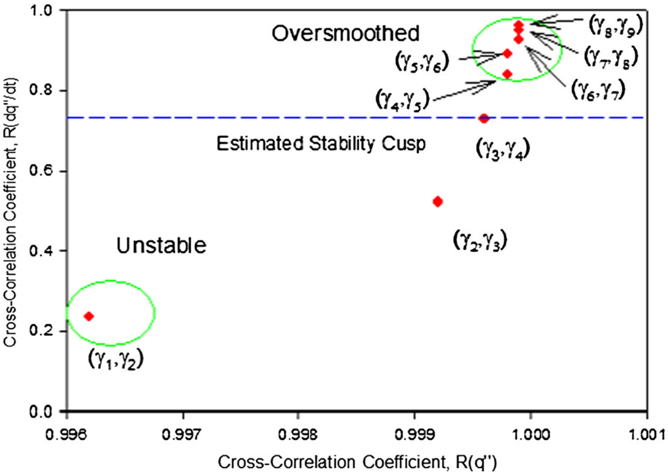

Fig. 14. Heat flux cross-correlation coefficient phase plane.

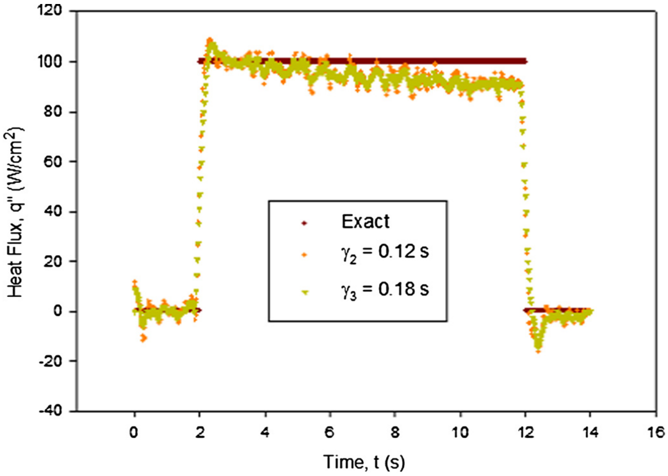

Fig. 15. Best estimates of heat flux.

5. Conclusions

This exploratory study presents the ground work for developing a new multi-layer, explosively-bonded, calorimeter for hostile testing environments. Heat flux gauge accuracy, based on calorimetry, requires a carefully formulated and resolvable data reduction equation relating in-depth transient temperature measurements to the net surface heat flux. This is a formidable task owing to a large temperature ranges and substantial heat fluxes generated in aerospace ground test facilities. In such cases, temperature dependent thermophysical properties need to be accounted and integrated into the data reduction equation. This process requires integration of analysis and instrumentation strategies in the design process. Numerical results, based on synthetic input data, reveal several important findings. This paper illustrates the need for inclusive modeling in arriving at the data reduction equation for the heat flux gauge. Several important results are highlighted in this paper including the: (a) identification of data reduction model discrepancies; (b) significance of Volterra integral formulations for algorithm development; (c) development of the approximation thread for uncertainty propagation; (d) achievement of stability through the future-time method; and, (e) extraction of the optimal regularization parameter through phase-plane and cross-correlation concepts for estimating the "best" heat flux. The next step in the process involves developing an instrumentation plan and computational methodology that can be integrated into a data reduction equation that takes advantage of the presented findings.

Declaration of competing interest

The authors declare that they have no known competing financial interests or personal relationships that could have appeared to influence the work reported in this paper.

Acknowledgements

The work reported here was supported by a grant provided to Dr. J.I. Frankel from the National Science Foundation (NSF-CBET-1703442).

References

[1] T.E. Diller, Advances in Heat Flux Measurements, Advances in Heat Transfer, vol. 23, Academic Press, NY, 1993, pp. 279–368.

[2] A. Gulhan, Heat Flux Measurements in High Enthalpy Flows, Defense Technical Information Center, ADP010750, April 2000, pp. 1–18, Identifier DTIC ADP010750, Identifier-ark ark:/13960/t54f5h62n.

[3] O. Chazot, Experimental Studies on Hypersonic Stagnation Point Chemical Environment, NATO, RTO-EN-AVT-142, 2007, pp. (13-1)–(13-32).

[4] I. Terraza-Salinas, Test Planning Guide for NASA Ames Research Center Arc Jet Complex and Range Complex, A029-9701-XM3 Rev.D, Ames Research Center, Thermophysics Facilities Branch, 8 January 2019, p. 37.

[5] W. Qiu, L.I. Jiwei, L.I. Jinping, Z. Wei, Z. Jiang, Performance of copper calorimeter for heat transfer measurement in high enthalpy shock tunnel, J. Therm. Eng. 27 (4) (2018) 373–381, https://doi.org/10.1007/s11630-018-1020-5.

[6] A. Nawaz, S. Gorbunov, I. Terraza-Salinas, S. Jones, Investigation of slug calorimeter gap influence for plasma stream characterization, in: 43rd AIAA Thermophysics Conference, 25-28 June 2012, New Orleans, LA, Paper AIAA-2012-3186.

[7] T.M. Hightower, R.A. Olivares, D. Philippidis, Thermal Capacitance (Slug) Calorimeter Theory including Heat Losses and Other Decaying Processes, NASA/TM -2008-215364, TFAWS 0801001, September 2008.

[8] M.N. Ozisik, Heat Conduction, Wiley, NY, 1980, pp. 1–24.

[9] V.S. Arpaci, Conduction Heat Transfer, Addison-Wesley, Reading, PA, 1966, pp. 1–82.

[10] R. Kress, Linear Integral Equations, 3rd ed., Springer-Verlag, New York, 1989, pp. 221–267.

[11] M. Wing, A Primer on Integral Equations of the First Kind, SIAM, Philadelphia, PA, 1991, pp. 1–38.

[12] J.V. Beck, B. Blackwell, C.R. St. Clair Jr., Inverse Heat Conduction, Wiley, NY, 1985, pp. 1–50.

[13] K. Kurpisz, A. Nowak, Inverse Thermal Problems, Computational Mechanics Publ., Southampton, England, UK, 1995, Chapters 1, 2.

[14] M.N. Ozisik, H.R.B. Orlande, Inverse Heat Transfer: Fundamentals and Applications, Taylor and Francis, New York, 2000.

[15] K.A. Woodbury, Effect of thermocouple sensor dynamics on surface heat flux predictions obtained via inverse heat transfer analysis, Int. J. Heat Mass Transf. 33 (12) (1990) 2641–2649, https://doi.org/10.1016/j.ijheatmasstransfer.2019.05.098.

[16] J.I. Frankel, H.C. Chen, Analytical developments and experimental validation of a thermocouple model through an experimentally acquired impulse response function, Int. J. Heat Mass Transf. 141 (2019) 1301–1314, https://doi.org/10.1016/j.ijheatmasstransfer.2019.05.098.

[17] J.I. Frankel, H.C. Chen, M. Keyhani, New step response formulation for inverse heat conduction, J. Thermophys. Heat Transf. 31 (4) (2017) 989–996, https://doi.org/10.2514/1.T5067.

[18] J.I. Frankel, H.C. Chen, Heat flux data reduction using a pre-conditioner test function for thin film analysis, AIAA J. Thermophys. Heat Transf., online available, https://doi.org/10.2514/1.T5744.

[19] D.L. Schultz, T.V. Jones, Heat Transfer Measurements in Short-Duration Hypersonics Facilities, NATO, AGARD-AG-165, 1973, pp. 1–55.

[20] T. Vanyai, Dynamic Calibration of Heat Transfer Gauges, M.S. Thesis, University of Oxford, October 2015.

[21] J.I. Frankel, Lecture Notes for ME, vol. 610, University of Tennessee, Knoxville, 2018.

[22] https://www.nobelclad.com/en/process. (Accessed 31 December 2019).

[23] J.M.H. Olmsted, Advanced Calculus, Appleton-Century-Crofts, NY, 1961, p. 117, pp. 321–324.

[24] P. Linz, Analytical and Numerical Methods for Volterra Equations, SIAM, Phila., PA, 1985, pp. 19–21, pp. 71–74, p. 130.

[25] J.I. Frankel, Regularization of inverse heat conduction by combination of rate sensors analysis and analytic continuation, J. Eng. Math. 57 (2007) 181–198, https://doi.org/10.1007/s10665-006-9073-y.

[26] I.N. Sneddon, Fourier Transforms, Dover, NY, 1995, pp. 29–31.

[27] J.I. Frankel, M. Keyhani, B. Elkins, Surface heat flux prediction through physics-based calibration - Part 1: theory, AIAA J. Thermophys. Heat Transf. 27 (2) (2013) 189–205, https://doi.org/10.2514/1.T3917.

[28] https://www.omega.com/en-us/resources/thermocouple-types. (Accessed 28 December 2019).

[29] J.I. Frankel, M. Keyhani, Phase-plane analysis and cross-correlation for estimating optimal regularization parameters in inverse heat conduction problems, AIAA J. Thermophys. Heat Transf. 28 (3) (2014) 542–548, https://doi.org/10.2514/1.T4357.

[30] J.I. Frankel, M. Keyhani, Cross correlation and inverse heat conduction by a calibration method, AIAA J. Thermophys. Heat Transf. 31 (3) (2017) 746–756, http://arc.aiaa.org/doi/abs/10.2514/1.T5059.